

22 **Abstract.** Using the vertical velocity (w) observed by a Ka-band millimeter wave cloud radar (MMCR)
23 at Wuhan, we investigate the evolution of convective boundary layer height (CBLH) based on a specified
24 threshold of vertical velocity variance (σ_w^2). The CBLHs from the MMCR w in the selected durations are
25 compared with those estimated by the lidar range corrected signal (RCS) and radiosonde temperature based
26 on different algorithms, showing good agreement with each other. Although these algorithms are on basis of
27 different dynamic and thermodynamic effects, the diurnal evolution of CBLH from MMCR is generally
28 consistent with that from lidar, except for a few hours post-sunrise and pre-sunset due to the influence of
29 aerosol residual layer on the lidar RCS. Meanwhile, the CBLH from MMCR shows less variation in
30 occurrence of sand and dust, and swifter response of thick clouds, relative to that from lidar. In this case,
31 σ_w^2 of the MMCR w identifies the CBLH based on dynamic effect, which can accurately capture the
32 diurnal evolution of CBLH compared with that from the change of long time-mixing aerosol concentration.
33 The monthly and seasonal features of CBLH at Wuhan is revealed via the MMCR measurement. Hence,
34 considering that the MMCR is capable of continuous observation in various weather conditions, the MMCR
35 w with high resolution can be applied to monitoring the evolution of CBLH in different atmospheric
36 conditions, which is helpful for improving our comprehensive understanding of CBL and dynamic processes
37 in CBL.

38

39 1. Introduction

40 The planetary boundary layer (PBL) is located in the lower part of the troposphere, and is where the
41 air-land (or air-sea) interaction takes place, thus the PBL is directly impacted by the surface forcings (Stull,
42 1988). Owing to the combined effects of friction, evaporation and transpiration, heat transfer, and pollutant
43 emission, the PBL is characterized by complex dynamical processes, with the prominent turbulence features
44 of vorticity and compressibility (Bernardini et al., 2012; Schneider, 2008). The height of PBL varies with

45 local time, ranging generally from a few tens of meters to a few kilometers at mid latitudes. Since the PBL
46 regulates the exchange of momentum, moisture and mass between the ground and the free atmosphere
47 (Mahrt, 1999; Holtslag and Nieuwstadt, 1986), the structure of PBL is an important input variable in
48 numerical weather-prediction and climate models (Edwards et al., 2020).

49 The convective boundary layer (CBL) is a type of PBL driven primarily by convection, and the CBL
50 height (CBLH) has a distinct daily cycle. Convective sources include heat transfer from the ground surface
51 warmed by solar radiation, and radiative cooling-induced air sinking from the cloud top, thus the evolution
52 of CBL is mainly dominated by surface sensible heat, which is significantly influenced by weather
53 conditions, such as clouds, and humidity near the surface (Kwon et al., 2022; Ribeiro et al., 2018; Zhang et
54 al. 2014). On a clear day, the CBLH rises after sunrise and reaches its maximum in the afternoon (LeMone
55 et al., 2010; Grossman and Robert, 2005; Yates et al., 2001). When the CBL collapses after sunset, most of
56 aerosol particles within the CBL are deposited into the nocturnal stable PBL due to the rapid weakening of
57 convectively driven turbulence, and some particles are transformed into an aerosol residual layer. The
58 residual layer descends gradually due to the sinking effect until it is mixed with the CBL driven by the next
59 day's post-sunrise convection (Blay-Carreras et al., 2014; Heus et al., 2010; Tennekes and Driedonks, 1981).
60 At the CBL top, moisture, aerosols and other chemical substances can be entrained to the free atmosphere,
61 leading to an entrainment transition zone between the CBL and the free atmosphere (Franck et al., 2021; Liu
62 et al., 2021; Brooks and Fowler, 2007). Hence, the CBL has an influence not only on the dispersion of
63 surface emissions and pollutants (Kong and Yi, 2015; Pal et al., 2015; Stull, 1988), but also on the weather
64 processes above it through the entrainment process (Guo et al., 2017; Brooks and Fowler, 2007; Neggers et
65 al., 2004).

66 The observations of in situ radiosonde and remote sensing are extensively used to estimate the CBLH
67 and its seasonal features. Radiosonde can obtain high-precision meteorological parameters, such as

68 temperature, humidity, horizontal wind and pressure, providing the possibility of estimating CBLH through
69 various algorithms (Seidel et al., 2010; Seibert, 2000). Typically, the vertical gradients of potential
70 temperature and water vapor (including relative humidity and specific humidity) are used to determine the
71 CBLH (Zhang et al., 2022; Guo et al., 2021; Dang et al., 2019; Liu and Liang, 2010; Seidel et al., 2010).
72 Additionally, the CBL top can be evaluated using the profiles of refractivity and bulk Richardson number
73 derived from the temperature, pressure, vapor pressure and horizontal wind data (Burgos-Cuevas et al., 2021;
74 Guo et al., 2016; Zhang et al., 2014; Seidel et al., 2012; Basha and Ratnam, 2009). These retrieval
75 algorithms provide insights into the features of CBL from the perspective of energy exchange, mass
76 transport, turbulent motion and effect on radio propagation. Even so, radiosonde faces a severe limitation in
77 capturing the clear development of CBL due to its conventional release schedule, which typically occurs
78 only twice a day.

79 In contrast to radiosonde, ground-based remote sensing offers high-temporal resolution in observational
80 profiles, which is essential to investigate the diurnal evolution of CBL. Wind profile radar can measure the
81 atmospheric wind speed and direction by analyzing the Doppler shift of the backscattered waves of multiple
82 beams (Liu et al., 2019; Singh et al., 2016; Seibert, 2000). The electromagnetic beams are reflected back due
83 mainly to the atmospheric refractive index change caused by the non-uniform vertical structure of the
84 atmosphere, such as vertical gradients in temperature, humidity, and turbulence, thus received echo and
85 retrieved wind from radar contain the information related to the atmospheric vertical structure. In this way,
86 several parameters from the wind profile radar measurement, such as signal-to-noise ratio, Doppler spectral
87 width, and refractive index structure constant, are utilized to retrieve the CBLH for every 30-60 minutes
88 based on their vertical gradients or chosen thresholds (Burgos-Cuevas et al., 2023; Bianco et al., 2022;
89 Solanki et al., 2021; Allabakash et al., 2017; Sandeep et al., 2014). Nevertheless, previous studies showed
90 that the top of CBL derived from the radar observation may be influenced by strong residual layer and

91 shallow or large entrainment zone (Sandeep et al., 2014; Bianco and Wilczak, 2002).

92 Lidar is regarded as a powerful detection equipment for capturing the CBL development due to its high
93 sensitivity to echo signals from various atmospheric components. Its relatively short operating wavelength
94 allows it to receive echoes backscattered not only from aerosol and cloud particles, but also from
95 atmospheric molecules. Nevertheless, since Rayleigh scattering of atmospheric molecules is much weaker
96 than Mie scattering of aerosol particles, the profile of lidar backscatter coefficient or range corrected signal
97 (RCS) from aerosols is applied to determining the CBLH by tracing the height where the aerosol
98 concentration sharply decreases with height. Accordingly, many techniques have been developed to identify
99 the extreme value of RCS gradient (Liu et al., 2021; Su et al., 2020; Dang et al., 2019; Yang et al., 2017;
100 Granados-Muñoz et al., 2012). As a simplified low-power lidar, ceilometer is initially designed to measure
101 the height of cloud base, thus similarly, the backscatter profile in the ceilometer observation can be
102 employed in the CBL investigation (Zhang et al., 2022; Schween et al., 2014; Van Der Kamp and McKendry,
103 2010). However, due to the incapability of lasers to penetrate clouds, the CBLH may be contaminated and
104 even misinterpreted by clouds within the CBL in the lidar and ceilometer measurements (Schween et al.,
105 2014).

106 With the advances in atmospheric sounding technology, the vertical velocity from Doppler lidar provides
107 a direct estimation of CBLH, which can reduce the impact of strong aerosol concentration within the
108 residual layer on the retrieved CBLH (Burgos-Cuevas et al., 2023; Dewani et al., 2023; Huang et al., 2017;
109 Schween et al., 2014; Barlow et al., 2011). At the initial stage of CBL formation in the morning and the
110 rapid decline stage of CBL in the late afternoon (Dewani et al., 2023; Manninen et al., 2018; Schween et al.,
111 2014; Barlow et al., 2011), aerosol particles in the residual layer may cause the CBLH to be overestimated
112 several hundred meters. This discrepancy is due to aerosols from a long time-mixing process rather than the
113 current situation of convectively driven turbulence (Burgos-Cuevas et al., 2023; Schween et al., 2014;

114 Pearson et al., 2010). When utilizing Doppler lidar data, a specified threshold of vertical velocity variance is
115 used to define the height of CBL top. This method has been validated by comparison with the radiosonde
116 observation (Dang et al., 2019; Li et al. 2017; Granados-Muñoz et al., 2012), and the sensitivity of threshold
117 has been discussed across different sites (de Arruda et al., 2018; Manninen et al., 2018; Schween et al., 2014;
118 Barlow et al., 2011; Pearson et al., 2010). A disadvantage of lidar is that it has a large blind range and
119 incapability to penetrate clouds, thus because of that, it is valuable to utilize microwave cloud radar that
120 offers good low altitude coverage and superior performance in cloud penetration. In the cloud observation, a
121 weak echo layer always exists near the surface, from which the vertical velocity can be retrieved. However,
122 there are few reports utilizing vertical velocity obtained from Doppler cloud radar for the CBL
123 investigations.

124 In present study, we estimate the CBLH based on the vertical velocity from a Ka-band millimeter wave
125 cloud radar (MMCR) at Wuhan, and compared this result with that derived from the lidar RCS by three
126 algorithms, and from radiosonde data by two algorithms. These algorithms are on basis of different dynamic
127 and thermodynamic effects, respectively, thus the comparison enhances our comprehensive understanding of
128 CBL and retrieval algorithms. Then, the general features of monthly and seasonal mean CBLHs are studied
129 by using the MMCR observation with high-temporal resolution. In section 2, the MMCR, lidar and their
130 data are briefly described. In Section 3, we discuss the methods that are used to identify the CBL top from
131 the MMCR, lidar and radiosonde measurements. In section 4, we present four examples of CBLH diurnal
132 evolution in different seasons by comparing the CBL tops retrieved from the MMCR and lidar
133 measurements, and then investigate the monthly and seasonal mean CBLHs over Wuhan in Section 5.
134 Section 6 provides a summary.

135

136 **2. Instruments and Data**

137 In this study, the CBLH derived from the MMCR measurements is compared with that from the lidar
138 measurements. The Ka-band MMCR and lidar are situated at the Atmospheric Remote Sensing Observatory
139 (ARSO) in Wuhan University (WHU, 30.5°N, 114.4°E). Wuhan, an inland megacity in central China, is
140 located in the east of Jiangnan Plain, with a resident population of over 12 million. The climate of the city is
141 humid, dominated by the subtropical monsoon, which is characterized by abundant precipitation and four
142 distinct seasons (Guo et al., 2023). Due to heavy traffic and industrial activities, large amounts of aerosols
143 are emitted from the industrialized metropolis. Sandstorms from the northwest often pass through Wuhan,
144 especially in spring. These sandstorms cause the remarkable variation in the spatial distribution and
145 concentration of aerosols. Frequent sand and dust activity along with cloudy weather poses significant
146 challenges for the Ka-band MMCR and lidar in accurately capturing the CBL evolution.

147 **2.1 Ka-Band Radar**

148 The WHU-CW MMCR established by the ARSO adopted a continuous wave (CW) system, and is a
149 Ka-band frequency-modulated continuous wave (FMCW) Doppler radar. The MMCR is installed in WHU,
150 as shown in Figure 1. The radar system transmits a mean power of 50 W at operating frequency of 35.035
151 GHz through 0.38° width beam formed by a Cassegrain antenna with 1.5 m diameter. Backscatter echoes
152 from aerosol and cloud particles are received by the other same Cassegrain antenna, and then are sent to the
153 signal processing subsystem to obtain the radial distribution of parameters that represent the characteristics
154 and motion of particles, such as reflectivity factor, Doppler velocity, and Doppler spectrum width. Because
155 of almost continuous transmitting and receiving, FMCW radar has generally a much higher mean power
156 relative to pulse radar, which improves the capacity of MMCR to detect weak echo targets. Meanwhile, by
157 modulating and demodulating the continuous wave, the FMCW radar measurement has an adjustable range
158 and time resolution. In non-precipitation, the MMCR measurement has a temporal resolution of 0.26 s and a
159 maximum measurable velocity of 4.30 m s⁻¹ without aliasing effect, which are adjusted to be 0.104 s and

160 10.75 m s⁻¹ in precipitation as the size and falling speed of hydrometeors increase (Mao et al., 2023),
161 respectively. The MMCR observation has been applied to the investigations of cloud and precipitation over
162 Wuhan in previous works (Fang et al., 2023; Mao et al., 2023).

163 The MMCR has a maximum detectable distance of about 30 km and a sensitivity of -30 dBZ at the
164 distance of 10 km. In the MMCR measurement, there are weak echoes generally less than -40 dBz within a
165 few kilometers above the surface. The weak echoes near the surface are attributed to the backscattering of
166 small insects and aerial plankton in some studies (Franck et al., 2021; Chandra et al., 2010; Achtemeier,
167 1991), and are also suggested to come from the scattering of dust particles in other studies (Görsdorf et al.,
168 2015; Clothiaux et al, 2000; Moran et al., 1998). Considering that the size of large dust particles, plant
169 aerosol particles, and aerosol particles from combustion can be much larger than 10 μm, it is possible for the
170 large aerosol particles to cause these weak echoes observed by MMCR. The servo-mechanical subsystem
171 conducts the MMCR to work in specified directional mode or scanning mode. In 2020, the MMCR was
172 operated in the vertical pointing mode, and the observation is recorded with a vertical resolution of 30 m. In
173 this study, we attempt to explore the CBL evolution at Wuhan from the Ka-band MMCR observation in
174 2020.

175 **2.2 Polarization Lidar**

176 The WHU-PL polarization lidar developed by the ARSO is also located in WHU, about 0.5 km from the
177 Ka-band MMCR. The lidar telescope is 70 m above sea level, which is about 30 m higher than the MMCR
178 antenna. Expanded laser beam overlaps with the full view field of the receiving telescope at a height of 0.3
179 km, thus this height is the low limit of lidar detection. The lidar data has a temporal resolution of 1 min, and
180 the same vertical resolution of 30 m as the MMCR data. In this study, we regard the height of MMCR
181 antenna as a baseline, and then the initial height of lidar data is set at 0.33 km.

182 The lidar system consists of transmitting subsystem receiving subsystem and information processing

183 subsystem. The lidar vertically emits the laser pulses of 120 mJ at operating wavelength of 532 nm with a
184 repetition rate of 20 Hz by a frequency-doubled Nd: YAG laser. The output polarized laser beam has a fine
185 polarization purity with depolarization ratio less than 1:10000 by using a Brewster polarizer. Light
186 backscattered by aerosol and cloud particles and atmospheric molecules is collected by a telescope with 0.3
187 m diameter. After separated through an interference filter with 0.3 nm bandwidth centered at 532 nm, the
188 elastically backscattered light is incident on a polarization beam splitter prism, and then the two-channel
189 polarized light are focused onto two photomultiplier tubes (PMTs), respectively. The signals from the two
190 PMTs are transferred to a personal computer (PC)-controlled two-channel transient digitizer, which can
191 obtain the echo signal intensity and volume depolarization ratio through the PC processing. Backscatter
192 coefficient is retrieved based on the backward iteration algorithm under the condition of a given lidar ratio
193 proposed by Fernald and Klett (Fernald, 1984; Klett, 1981), and then the RCS is derived from the
194 backscatter coefficient (Freudenthaler et al., 2009; Immler and Schrems, 2003). The lidar configuration and
195 depolarization comparison with the measurement from the cloud-aerosol lidar and infrared pathfinder
196 satellite observation (CALIPSO) were in detail described in the early study (Kong and Yi, 2015).

197

198 **3. Methodology**

199 Given that the CBLH is estimated from instruments that retrieve different variables, the algorithms that
200 are utilized to make such estimations are also based on different principles, which are explained in the
201 following subsections.

202 **3.1 Gradient, Variance and Wavelet Transformation Methods**

203 In the lidar observation, the CBLH is derived from the RCS, which is approximately proportional to the
204 aerosol concentration (Kong and Yi, 2015; Lewis et al., 2013; Pal et al., 2010; Emeis et al., 2008). Generally,
205 aerosols are well-mixed within the CBL due to the convectively driven turbulence, and its concentration

206 decays sharply over the CBL top. Hence, the gradient (Grd) method is often utilized to investigate the
207 CBLH by identifying the strongest or minimum gradient of RCS. The wavelet covariance transformation
208 (WCT) method, with a chosen Harr wavelet function, estimates the CBL top by investigating the correlation
209 of the RCS variation with a step function (Zhang et al., 2021; Angelini and Gobbi, 2014; Pal et al., 2010;
210 Baars et al., 2008; Brooks, 2003). Essentially, the WCT method can be considered as a smooth enhancement
211 of Grd method, which may be less affected by noise than the Grd method (Davis et al., 2000; Baars et al. al.,
212 2008).

213 On the other hand, because of the entrainment process, there is a frequent exchange of matter and energy
214 between the CBL and the free atmosphere, causing the dramatic variation of aerosol concentration or lidar
215 RCS on small time scales around the CBL top (Zhang et al., 2018; Kong and Yi, 2015). In this case, the
216 variance (Var) method is used to determine the CBL top by identifying the maximum variance of RCS
217 during a relatively long period (Lammert and Bösenberg, 2006; Martucci et al., 2004; Piironen and Eloranta,
218 1995). We estimate the CBLH from the lidar RCS in a period of 30 min by using the three methods, for
219 instance, the CBLH at 12:00 LT (the same below) is calculated based on the RCS data from 11:45 to 12:15.

220 **3.2 Threshold Method**

221 The variance (σ_w^2) of vertical velocity (w) is representative of the level of turbulent activity, thus a
222 threshold of σ_w^2 is applied to determining the CBLH in the Doppler lidar measurement. The threshold is
223 chosen to be $0.04 \text{ m}^2 \text{ s}^{-2}$ in the regions with weak turbulence (Tucker et al., 2009), $0.3 \text{ m}^2 \text{ s}^{-2}$ in a tropical
224 rainforest (Pearson et al., 2010), and $0.4 \text{ m}^2 \text{ s}^{-2}$ in the regions with central European climate (Schween et al.,
225 2014; Träumner et al., 2011), while the thresholds of 0.1 and $0.2 \text{ m}^2 \text{ s}^{-2}$ are selected in the urban landscapes
226 since the retrieved CBLH is not heavily dependent on the given thresholds (Burgos-Cuevas et al., 2023;
227 Huang et al. 2017; Barlow et al., 2011). Similarly, the threshold method is also used to determine a CBLH
228 from the more than 6000 w profiles in the MMCR measurement during a period of 30 min.

229 Figure 2 presents the distribution of w from the Ka-band MMCR observation and RCS (in arbitrary
230 unit) from the lidar measurement on 15 August 2020. The day is 3 days later than the rainy day of 12 August.
231 By taking observations for a period of 30 min from 11:45 to 12:15, we calculate the mean w and RCS, and
232 estimate the position of CBL top by means of different algorithms, which are shown in Figure 3. From the
233 lidar RCS, the CBLH is 1.35 km in the Grd and WCT methods, and 1.32 km in the Var method. In the
234 MMCR observation, σ_w^2 has a clear downward trend with increasing height, with the values of about 1.36
235 $\text{m}^2 \text{s}^{-2}$ from the near ground to 0.15 $\text{m}^2 \text{s}^{-2}$ at 1.47 km, and then maintains slight fluctuations around the value
236 of 0.15 $\text{m}^2 \text{s}^{-2}$ to higher altitudes. For a specified threshold of 0.3 $\text{m}^2 \text{s}^{-2}$, the CBL top is identified at the
237 height of 1.35 km, which is in agreement with the lidar results.

238 It can be noted from Figures 3d and 3f that the CBLHs in the mean RCS profile are around the position
239 with the most rapid change, while the CBLH retrieved from the MMCR σ_w^2 is not related to the vertical
240 variation of mean w . σ_w^2 indicates the turbulence level under the current condition, whereas, RCS tends to
241 reflect the variation in the concentration of long time-mixing aerosol particles caused by dynamic effects
242 (Kotthaus et al., 2023). Hence, the threshold method is a dynamical algorithm, which is more effective in
243 capturing the dynamic changes within the CBL compared to the aerosol concentration algorithm based on
244 the lidar RCS. In this way, the MMCR observes the high-temporal resolution data of w , making it available
245 for analyzing diurnal evolution of CBL in different months and seasons. However, based on earlier studies,
246 the selected threshold values are subject to change across the different regions (Burgos-Cuevas et al., 2023;
247 Schween et al., 2014; Pearson et al., 2010; Tucker et al., 2009).

248 In Figure 3e, σ_w^2 decreases quickly from 0.4 $\text{m}^2 \text{s}^{-2}$ at 1.29 km to 0.15 $\text{m}^2 \text{s}^{-2}$ at 1.47 km, indicating that
249 the CBH top at noon is less sensitive to the selected threshold within 0.15-0.4 $\text{m}^2 \text{s}^{-2}$. Figure 4 depicts the
250 CBLHs on 15 August 2020 at the thresholds from 0.2 to 0.45 $\text{m}^2 \text{s}^{-2}$. Nevertheless, the CBLH from 09:30 to
251 17:30 remains relatively stable with little change at the different thresholds, and the discrepancy among

252 these thresholds arises mainly in the initial growing and final decaying stages of CBL.

253 σ_w^2 of MMCR w determines the CBL top from the perspective of dynamic effect, and the CBLH can
254 be estimated from the temperature data based on the thermodynamic effect. Here, we compare the CBLH
255 derived from the MMCR w with that from the radiosonde data. Radiosonde is typically launched in
256 Wuhan at 08:00 and 20:00. Given that the sun has set by 20:00, we present the comparison at 08:00. The
257 radiosonde data are provided by University of Wyoming from the website at
258 <https://weather.uwyo.edu/upperair/buffraob.shtml>. The vertical resolution of radiosonde data in Wuhan was
259 approximately 0.5-1.0 km before June 2021, and then was improved to a range of tens to hundreds of meters
260 at higher altitudes. Therefore, we select the high-resolution data in the days without precipitation for our
261 analysis.

262 We estimate the CBLH from the radiosonde data by using the methods of potential temperature (θ)
263 gradient and bulk Richardson number (Ri) threshold. The potential temperature gradient (Grd_θ) is
264 calculated at two adjacent heights in the radiosonde data, and the CBLH is determined by the maximum
265 gradient in the profile of Grd_θ (Seidel et al., 2010). The bulk Richardson number is expressed (Zhang et al.,
266 2014; Seibert et al., 2000), as follows,

$$267 \quad Ri(z) = \frac{(g/\theta_{vs})(\theta_{zs} - \theta_{vs})z}{(u_z - u_s)^2 + (v_z - v_s)^2 + (bu_s^2)} \quad (1)$$

268 where g is the acceleration due to gravity; z is the height; θ_v is the virtual potential temperature; u_* is
269 the surface friction velocity; u and v are the zonal and meridional wind components, respectively; and
270 b is a constant, which is usually set to zero due to the fact that friction velocity is much weaker compared
271 with the horizontal wind (Seidel et al., 2012). The subscripts of z and s denote the parameters at z
272 height and surface level, respectively. In the profile of Ri , the CBLH is identified when Ri firstly crosses
273 a threshold value upward from the ground, and the threshold is typically taken as 0.25 in early studies (Guo

274 et al., 2021; Seibert et al., 2000), which is chosen in the analysis.

275 Figure 5 shows the comparisons of CBLHs derived from the MMCR and radiosonde measurements at
276 8:00 on 21 and 25, July 2021, respectively. On 21, for a threshold of $\sigma_w^2=0.3 \text{ m}^2 \text{ s}^{-2}$, the CBLH of 0.39 km
277 from the MMCR w is in agreement with that of 0.40 km from the radiosonde Grd_θ , which are slightly
278 larger than that of 0.34 km from the radiosonde Ri . In contrast to this, on 25, the CBLH is 0.57 km from
279 the MMCR w , which is consistent with that of 0.59 km from the radiosonde Ri , but is slightly higher than
280 that of 0.45 km from the radiosonde Grd_θ . Nevertheless, in the whole, the results from all the three
281 methods roughly agree with each other.

282 Figure 6 displays the scatterplot of CBLHs identified by the MMCR w , and the radiosonde Grd_θ
283 and Ri at 8:00 on the clear days in June and July 2021. The different variables and algorithms are used in
284 the three methods, thus there are some differences of CBLHs derived from these methods, as shown in
285 Figure 6. The CBLH from σ_w^2 of MMCR w has the correlation coefficients of 0.83 and 0.81 with that
286 from the radiosonde Grd_θ and Ri , respectively, which are highly consistent with the correlation
287 coefficient of 0.83 from the radiosonde Grd_θ and Ri . These results support the threshold of $\sigma_w^2 = 0.3 \text{ m}^2$
288 s^{-2} applied to the CBLH estimation in Wuhan. In following analysis, we take $0.3 \text{ m}^2 \text{ s}^{-2}$ as the threshold to
289 determine the CBLH in the MMCR observation.

290 It can be noted that the comparison focuses solely on the CBLH at 8:00 rather than the diurnal evolution
291 of CBLH, owing to the lack of radiosonde observation. Consequently, we analyze the diurnal evolution of
292 CBLH derived from the MMCR and lidar measurements.

293

294 4. Case Investigation and Comparison

295 Figure 7 presents the CBLH evolution on 15 August 2020 from the lidar RCS based on the Grd, Var and
296 WCT methods, and the comparison with that obtained from the MMCR σ_w^2 , together with the distribution

297 of MMCR reflectivity factor in the range of 10-15 km. As shown in Figure 7c, due to the influence of
298 aerosol residual layer, the CBLH from the lidar RCS fluctuates from about 1.56 km at 06:00 down to 1.17
299 km at 09:30, however, with the sunrise at 05:50, the CBL top derived from the MMCR σ_w^2 gradually rises
300 from about 0.09 km at 06:00 to 1.17 km at 09:30. It is interesting that the CBLH from the lidar RCS
301 variance drops at 07:30 and then shows a change similar to that from the MMCR σ_w^2 . Both the variances of
302 w and RCS represent the deviation degree of their small time scale values relative to their 30 min-mean
303 values, which may be responsible for the similar results. When the CBL ascends gradually and mixes with
304 the residual layer, the CBLHs in the lidar and MMCR observations are consistent with each other between
305 09:30 and 17:00, including a slight drop at 12:30 and 14:30 (from the gradient and variance of RCS). The
306 maximum height of CBL is about 1.71 km at 14:00 and 15:00 based on σ_w^2 and the RCS gradient and
307 variance.

308 One can note from the reflectivity factor distribution in Figure 7b that cirrus clouds occur from 17:00,
309 develop rapidly into the thick clouds at about 11-14.4 km at 17:30, and then dissipate quickly after 17:30. In
310 the MMCR observation, the CBLH shows an obvious reduction between 17:30 and 18:30, and then a lift as
311 the clouds dissipates rapidly. Earlier studies from the Doppler lidar w investigated the complex influence
312 of low-level clouds on the CBL and turbulence. The cloud-top radiative cooling drives top-down convective
313 mixing, leading to the increasement of σ_w^2 (Hogan et al., 2009; Harvey et al., 2013; Manninen et al., 2018).
314 Whereas, during the warm season, the magnitude of σ_w^2 from the lidar w is large on clear-sky days and
315 decreases on cloud-topped days, and the intensity of turbulence reduces with an increase in the cloud
316 fraction within the CBL, except in the cloud layer that exceeds 90% of the CBL thickness (Dewani et al.,
317 2023). Here, the cirrus clouds are above 11 km, thus the cloud-top driven convective mixing has little impact
318 on the low atmosphere, however, the thick clouds cool the surface by attenuating solar radiation, which can
319 weaken the surface-driven convective mixing. Therefore, the thick cirrus makes a large contribution to the

320 evident reduction of CBLH. The phenomenon of CBLH reduction also arises in the lidar RCS, especially
321 from the RCS variance, but with a time lag due to the influence of a long time-mixing process on the aerosol
322 distribution (Burgos-Cuevas et al., 2023; Schween et al., 2014). After the sunset at 19:05, the CBLH
323 retrieved by σ_w^2 drops quickly to 0.27 km at 20:00 from 1.47 km at 19:00, while the top of aerosol residual
324 layer (or horizontally migrating aerosol layer) identified by the lidar stays at a far higher level, especially
325 from the RCS gradient and WCT.

326 Next, we select the observations on 31 January, 12 November, and 19 March 2020 to compare the CBLH
327 evolutions. The three days, without clouds and precipitation, are chosen as the representative in different
328 seasons. Figure 8 shows the CBLHs on 31 January derived from the four methods above, which are overlaid
329 on the MMCR w and σ_w^2 and the lidar RCS, respectively. January is the coldest month of the year, and
330 on 31 January, the minimum (maximum) temperature is -5 °C (4 °C) recorded in the weather forecast.
331 Owing to the convection inhibited largely by the frigid surface and air, σ_w^2 shows that the CBLH develops
332 very slowly upward to 0.3 km at 11:30 from 0.12 km at 07:30 as the sun rises at 07:15. Thereafter, the top of
333 CBL escalates quickly to 0.9 km at 13:30, and reaches the maximum height of 0.99 km at 14:30, and during
334 this period, the CBLH from the lidar RCS experiences a similarly rapid uplift, and attains the peak of 1.2 km
335 at 14:00 from the RCS gradient and variance, and 1.14 km at 14:30 from the RCS WCT. In addition, it can
336 be seen from Figure 8d that all the CBLHs from the lidar RCS are slightly larger than those from the
337 MMCR σ_w^2 , which may be attributed to the long time-mixing aerosols and wet surface in winter. After
338 14:30, the CBLH from σ_w^2 descends gradually, and approaches the ground at 17:30 prior to the sunset at
339 17:57, while at the sunset, the CBL top from the RCS is at 0.8-0.9 km due to the long time-mixing
340 processes.

341 Figure 9 presents the CBLHs determined from the MMCR and lidar observations on 12 November 2020.
342 With the sunset on this day in late autumn, the CBLH identified from σ_w^2 displays a little fluctuation until

343 10:30. After then, the CBL is rapidly developed to 0.51 km at 11:30, and mixes fully with the residual layer
344 retrieved from the lidar RCS, thus the CBL tops have approximately the same evolution between the MMCR
345 and lidar observations from 11:30 to 17:30, with the maximum values of about 0.75-0.78 km at 15:00 and
346 16:00. As the sun goes down at 17:27, the CBL from σ_w^2 rapidly shrinks close to the ground at 18:00, and
347 aerosol particles left in the air form a residual layer, similar to the two cases above.

348 Figure 10 depicts the CBLH variations in the MMCR and lidar observations on 19 March 2020, together
349 with the depolarization ratio from the lidar. In spring, sand and dust with different intensities from the
350 northwest of China pass frequently through Wuhan. On this day, there is a fine sand and dust layer mostly
351 above 1.8 km, with the depolarization ratios of about 0.08-0.12 in Figure 10c, which can also be noted from
352 the distribution of w in the MMCR observation. Meanwhile, another sand and dust layer with the larger
353 depolarization ratios of about 0.14-0.16 passes through Wuhan from about 14:00, and mixes with the lower
354 part of the first sand and dust layer. In this situation, the MMCR observation indicates that the CBL starts to
355 develop gently upward from the sunrise, and the upward trend of CBLH is also presented in the lidar
356 measurement, but at higher altitudes. At 09:30, the CBLH is about 0.48 km in both the MMCR and lidar
357 observations, and then rises steadily to 1.32 km at 16:00 and 16:30, showing a good agreement between the
358 two observations. Subsequently, the CBLH from σ_w^2 undergoes two rapid declines. One occurs from 1.2
359 km at 17:00 to 0.51 km at 18:00, which is probably related to the sand and dust deposition in addition to the
360 diminished radiation in the late afternoon, and the other arises after the sunset. However, because of the
361 effect of sand and dust, the CBLH from the lidar RCS increases slightly from 1.32 km at 16:30 to about 1.38
362 km at 18:00 and 18:30, and then decreases gradually with time.

363 The CBLH is identified by the spatial and temporal variation of aerosol concentration from the lidar
364 measurement and by the temporal change of w from the MMCR observation. The four examples
365 demonstrate that except for the periods with the influence of aerosol residual layer, particularly during the

366 few hours after sunrise and before sunset, the MMCR CBLHs are generally in agreement with the lidar
367 CBLHs. The residual layer causes a higher CBLH estimated by the lidar RCS than by the MMCR σ_w
368 because σ_w^2 is less contaminated by the residual layer relative to the aerosol concentration. Additionally,
369 the CBLH estimated by σ_w^2 shows a rapid response to thick high-level clouds and less influence by the
370 long-range transport of sand and dust. Hence, the MMCR observation can accurately retrieve the CBLH and
371 capture its diurnal evolution, especially for the CBL in the blind range of lidar.

372

373 **5. Monthly and Seasonal Mean CBLHs**

374 To reveal the general characteristics of CBLH diurnal evolution in different months and seasons, we
375 calculate the monthly and seasonal mean CBLHs by using the MMCR σ_w on these days without
376 precipitation in 2020. We consider that winter covers the months of December, January and February, while
377 March, April and May are spring, June, July and August are summer and the rest is autumn.

378 Figure 11 illustrates the averaged CBLHs with the standard deviations superimposed on the mean σ_w^2
379 in each month and season. As the spot of direct sunlight slowly moves northward, the mean variance
380 gradually increases from January to July, and then decreases gradually from August to December, moreover,
381 the coverage height and time duration of its large values show an analogous monthly variation. In this case,
382 the peak height of CBL ascends steadily from 0.66 km in January to 1.47 (1.44) km in July (August), and
383 subsequently, descends gradually to the lowest height of 0.42 km in December. Additionally, at Wuhan, the
384 plum rain starts in June and prevails in July. As shown in Figure 11, the CBLH in July has the largest
385 standard deviation (between 13:00 and 19:00), which is possibly attributable to the cloudy and rainy weather
386 besides the strongest radiation.

387 As for seasonal variation, as we expected, the mean σ_w^2 is the strongest in summer and the weakest in
388 winter. Interestingly, the variance is significantly larger in spring than in autumn. Not only the maximum

389 CBLH of 1.14 km at 13:30 in spring is much higher than that of about 0.66 km at 13:30 and 14:00 in autumn,
390 but also the mean σ_w^2 of 0.42 $\text{m}^2 \text{s}^{-2}$ in the CBL during spring is stronger than that of 0.35 $\text{m}^2 \text{s}^{-2}$ during
391 autumn. The maximum height of CBL is 1.29 km at 14:30 and 15:00 in summer, and about 0.6 km at 14:30
392 in winter. In summer, the CBLH displays a feature of quick descent near twilight, and in autumn, the CBL
393 shows a wider envelope with an earlier development and a later dissipation relative to that in winter though
394 their maximum CBLHs are almost the same. In previous studies, based on the threshold of σ_w^2 from the
395 Doppler lidar measurement in Mexico City (19.3° N, 99.1° E), the CBLH is higher in spring and summer,
396 and lower in winter, while the maximum CBLH of about 1.5 km occurs in May, which is because the CBLH
397 is suppressed to some extent by increased cloud cover in the rainy season between June and September
398 (Burgos-Cuevas et al., 2021). However, the CBLH retrieved from the ceilometer backscatter data is
399 obviously larger than that from the threshold of σ_w^2 (Burgos-Cuevas et al., 2021; Tang et al., 2016).
400 Similarly, in the estimation of CBLH from the lidar RCS over Wuhan and Granada (37.18° N, 3.60° E), the
401 maximum values of seasonal mean CBLHs in all the seasons are larger than those in our results although the
402 gradual ascent of CBLH from winter and autumn to spring and summer is consistent with that in our results
403 (Kong and Yi, 2015; Granados-Muñoz et al., 2012).

404

405 **6. Summary**

406 In this study, we estimate the CBLH from the profile of w in the Ka-MMCR observation by using a
407 threshold of σ_w^2 . The CBLH from MMCR is compared with that from the lidar RCS by utilizing the
408 gradient, variance and wavelet methods, and from radiosonde data by using the methods of θ gradient and
409 Ri , which demonstrates the general agreement of CBLH estimation based on different dynamic and
410 thermodynamic effects. Then, we investigate the diurnal evolution of monthly and seasonal mean CBLHs
411 based on the MMCR observation.

412 Although the RCS is proportional to aerosol concentration and w represents the vertical motion of
413 aerosol particles, the comparison of four examples in different seasons indicates that the diurnal evolution of
414 CBLH from the MMCR w is consistent with those from the lidar RCS, except for the initial growth and
415 final decay phases. The discrepancy can mainly be attributed to the aerosol residual layer and the lidar blind
416 range. The influence of residual layer on the lidar RCS generally causes an overestimation of CBLH,
417 meanwhile, it is impossible for lidar to capture the CBL top within its large blind range. In addition, the
418 CBLH in the MMCR observation shows less contamination by the long-range transport of sand and dust,
419 and thick high-level clouds due to the rapid response of aerosol w relative to its concentration. In this case,
420 the MMCR observation can capture the diurnal evolution of CBLH.

421 Using the profile of w from the MMCR observation on these days without precipitation in 2020, we
422 investigate the diurnal evolution of monthly and seasonal mean CBLHs. The maximum value of monthly
423 mean CBLH increases gradually from 0.66 km in January to 1.47 (1.44) km in July (August), and then
424 decreases to the lowest height of 0.42 km in December. As for the seasonal behavior, the mean CBLH has
425 the maximum heights of 1.29 km at 14:30 and 15:00 in summer, 1.14 km at 13:30 in spring, 0.66 km at
426 13:30 and 14:00 in autumn, and 0.6 km at 14:30 in winter. In addition, the statistical standard deviations are
427 monthly-dependent, indicating that the CBLH is not only mainly regulated by the surface heating associated
428 with solar radiation, but also significantly affected by weather conditions, such as humidity and clouds.
429 Therefore, since the Ka-band MMCR is a powerful instrument for observing clouds and weak precipitation,
430 the full-time MMCR observation with low blind height can obtain the entire diurnal evolution of CBLH,
431 which helps us gain an insight into CBL features and also provides important input variables for weather
432 prediction and climate models.

433

434

435 **Code availability.** Software code to obtain the results is available upon request from the corresponding
436 author.

437 **Data availability.** All data used are available upon request from the corresponding author.

438 **Author contributions.** KH and FY conceptualized this study. ZZ and KH completed the analysis and the
439 manuscript. WC, FL, JZ, YJ, and FY discussed the results and finalized the manuscript.

440 **Competing interests.** The authors declare that they have no conflict of interest.

441 **Financial support.** This work was supported by the National Key Research and Development Program of
442 China (2022YFF0503700 and 2022YFB3901800) and the National Natural Science Foundation of China
443 (42174189).

444 **Acknowledgements.**

445 We are grateful to the editor and reviewers for their valuable comments on our manuscript, and University
446 of Wyoming for providing the radiosonde data at the website of
447 <https://weather.uwyo.edu/upperair/bufrroob.shtml>.

448

449

450 **References**

451 Allabakash, S., Yasodha, P., Bianco, L., Venkatramana Reddy, S., Srinivasulu, P., and Lim, S.: Improved
452 boundary layer height measurement using a fuzzy logic method: Diurnal and seasonal variabilities of
453 the convective boundary layer over a tropical station, *J. Geophys. Res.-Atmos.*, 122, 9211–9232,
454 <https://doi.org/10.1002/2017JD027615>, 2017.

455 Achtemeier, G. L.: The use of insects as tracers for “Clear-Air” boundary-layer studies by doppler radar, *J.*
456 *Atmos. Ocean. Tech.*, 8, 746-765,
457 [https://doi.org/10.1175/1520-0426\(1991\)008<0746:TUOIAT>2.0.CO;2](https://doi.org/10.1175/1520-0426(1991)008<0746:TUOIAT>2.0.CO;2), 1991.

458 Baars, H., Ansmann, A., Engelmann, R., and Althausen, D.: Continuous monitoring of the boundary-layer
459 top with lidar, *Atmos. Chem. Phys.*, <https://doi.org/10.5194/acp-8-7281-2008>, 2008.

460 Barlow, J. F., Dunbar, T. M., Nemitz, E. G., Wood, C. R., Gallagher, M. W., Davies, F., O'Connor, E., and
461 Harrison, R. M.: Boundary layer dynamics over London, UK, as observed using Doppler lidar during
462 REPARTEE-II, *Atmos. Chem. Phys.*, 11, 2111–2125, <https://doi.org/10.5194/acp-11-2111-2011>, 2011.

463 Basha, G. and Ratnam, M. V.: Identification of atmospheric boundary layer height over a tropical station
464 using high-resolution radiosonde refractivity profiles: Comparison with GPS radio occultation
465 measurements, *J. Geophys. Res.-Atmos.*, 114, 2008JD011692, <https://doi.org/10.1029/2008JD011692>,
466 2009.

467 Bernardini, M., Pirozzoli, S., and Orlandi, P.: Compressibility effects on roughness-induced boundary layer
468 transition, *Int. J. Heat Fluid Fl.*, 35, 45–51, <https://doi.org/10.1016/j.ijheatfluidflow.2012.02.007>, 2012.

469 Bianco, L. and Wilczak, J. M.: Convective boundary layer depth: Improved measurement by doppler radar
470 wind profiler using fuzzy logic methods, *J. Atmos. Ocean. Tech.*, 19, 1745–1758,
471 [https://doi.org/10.1175/1520-0426\(2002\)019<1745:CBLDIM>2.0.CO;2](https://doi.org/10.1175/1520-0426(2002)019<1745:CBLDIM>2.0.CO;2), 2002.

472 Bianco, L., Muradyan, P., Djalalova, I., Wilczak, J. M., Olson, J. B., Kenyon, J. S., Kotamarthi, R., Lantz, K.,
473 Long, C. N., and Turner, D. D.: Comparison of observations and predictions of daytime
474 planetary-boundary-layer heights and surface meteorological variables in the Columbia river gorge and
475 basin during the second wind forecast improvement project, *Bound.-Lay. Meteorol.*, 182, 147–172,
476 <https://doi.org/10.1007/s10546-021-00645-x>, 2022.

477 Blay-Carreras, E., Pino, D., Vilà-Guerau De Arellano, J., Van De Boer, A., De Coster, O., Darbieu, C.,
478 Hartogensis, O., Lohou, F., Lothon, M., and Pietersen, H.: Role of the residual layer and large-scale
479 subsidence on the development and evolution of the convective boundary layer, *Atmos. Chem. Phys.*,
480 14, 4515–4530, <https://doi.org/10.5194/acp-14-4515-2014>, 2014.

481 Brooks, I. M.: Finding Boundary Layer Top: Application of a wavelet covariance transform to lidar
482 backscatter profiles, *J. Atmos. Ocean. Tech.*, 20, 1092–1105,
483 [https://doi.org/10.1175/1520-0426\(2003\)020<1092:FBLTAO>2.0.CO;2](https://doi.org/10.1175/1520-0426(2003)020<1092:FBLTAO>2.0.CO;2), 2003.

484 Brooks, I. M. and Fowler, A. M.: A new measure of entrainment zone structure, *Geophys. Res. Lett.*, 34,
485 2007GL030958, <https://doi.org/10.1029/2007GL030958>, 2007.

486 Burgos-Cuevas, A., Adams, D. K., García-Franco, J.L., and Ruiz-Angulo, A.: A seasonal climatology of the
487 Mexico City atmospheric boundary layer, *Bound.-Lay. Meteorol.*, 180, 131–154,
488 <https://doi.org/10.1007/s10546-021-00615-3>, 2021.

489 Burgos-Cuevas, A., Magaldi, A., Adams, D. K., Grutter, M., García-Franco, J. L., and Ruiz-Angulo, A.:
490 Boundary layer height characteristics in Mexico City from two remote sensing techniques, *Bound.-Lay.*
491 *Meteorol.*, 186, 287–304, <https://doi.org/10.1007/s10546-022-00759-w>, 2023.

492 Chandra, A. S., Kollias, P., Giangrande, S. E., and Klein, S. A.: Long-term observations of the convective
493 boundary layer using insect radar returns at the SGP ARM climate research facility, *J. Climate*, 23,
494 5699–5714, <https://doi.org/10.1175/2010JCLI3395.1>, 2010.

495 Clothiaux, E. E., Ackerman, T. P., Mace, G. G., Moran, K. P., Marchand, R. T., Miller, M. A., and Martner, B.
496 E.: Objective determination of cloud heights and radar reflectivities using a combination of active
497 remote sensors at the ARM CART sites, *J. Appl. Meteorol.*, 39, 645–665,
498 [https://doi.org/10.1175/1520-0450\(2000\)039<0645:ODOCHA>2.0.CO;2](https://doi.org/10.1175/1520-0450(2000)039<0645:ODOCHA>2.0.CO;2), 2000.

499 Dang, R., Yang, Y., Hu, X.-M., Wang, Z., and Zhang, S.: A review of techniques for diagnosing the
500 atmospheric boundary layer height (ABLH) using aerosol lidar data, *Remote Sens.-Basel*, 11, 1590,
501 <https://doi.org/10.3390/rs11131590>, 2019.

502 Davis, K. J., N. Gamage, C. Hagelberg, C. Kiemle, D. Lenschow, and P. Sullivan: An objective method for
503 deriving atmospheric structure from airborne lidar observations, *J. Atmos. Ocean. Tech.*, 17,

504 1455–1468, doi:10.1175/1520-0426(2000)017<1455:AOMFDA>2.0.CO;2, 2000.

505 de Arruda Moreira, G., Guerrero-Rascado, J. L., Bravo-Aranda, J. A., Benavent-Oltra, J. A., Ortiz-Amezcu,
506 P., Román, R., Bedoya-Velásquez, A. E., Landulfo, E., and Alados-Arboledas, L.: Study of the
507 planetary boundary layer by microwave radiometer, elastic lidar and Doppler lidar estimations in
508 Southern Iberian Peninsula, *Atmos. Res.*, 213, 185–195, <https://doi.org/10.1016/j.atmosres.2018.06.007>,
509 2018.

510 Dewani, N., Sakradzija, M., Schlemmer, L., Leinweber, R., and Schmidli, J.: Dependency of vertical
511 velocity variance on meteorological conditions in the convective boundary layer, *Atmos. Chem. Phys.*,
512 23, 4045–4058, <https://doi.org/10.5194/acp-23-4045-2023>, 2023.

513 Edwards, J. M., Beljaars, A. C. M., Holtslag, A. A. M., and Lock, A. P.: Representation of boundary-layer
514 processes in numerical weather prediction and climate models, *Bound.-Lay. Meteorol.*, 177, 511–539,
515 <https://doi.org/10.1007/s10546-020-00530-z>, 2020.

516 Emeis, S., K. Schäfer, and C. Münkel: Surface-based remote sensing of the mixing-layer height—A review,
517 *Meteorol. Z.*, 17, 621–630, <https://doi.org/10.1127/0941-2948/2008/0312>, 2008.

518 Fang, J., Huang, K., Du, M., Zhang, Z., Cao, R., and Yi, F.: Investigation on cloud vertical structures based
519 on Ka-band cloud radar observations at Wuhan in Central China, *Atmos. Res.*, 281, 106492,
520 <https://doi.org/10.1016/j.atmosres.2022.106492>, 2023.

521 Fernald, F. G.: Analysis of atmospheric lidar observations: Some comments, *Appl. Opt.*, 23, 652–653,
522 <https://doi.org/10.1364/AO.23.000652>, 1984.

523 Franck, A., Moisseev, D., Vakkari, V., Leskinen, M., Lampilahti, J., Kerminen, V.-M., and O’Connor, E.:
524 Evaluation of convective boundary layer height estimates using radars operating at different frequency
525 bands, *Atmos. Meas. Tech.*, 14, 7341–7353, <https://doi.org/10.5194/amt-14-7341-2021>, 2021.

526 Freudenthaler, V., Esselborn, M., Wiegner, M., Heese, B., Tesche, M., Ansmann, A., Müller, D., Althausen,

527 D., Wirth, M., Fix, A., Ehret, G., Knippertz, P., Toledano, C., Gasteiger, J., Garhammer, M., and
528 Seefeldner, M.: Depolarization ratio profiling at several wavelengths in pure Saharan dust during
529 SAMUM 2006, *Tellus B*, 61, 165, <https://doi.org/10.1111/j.1600-0889.2008.00396.x>, 2009.

530 Görsdorf, U., Lehmann, V., Bauer-Pfundstein, M., Peters, G., Vavriv, D., Vinogradov, V., and Volkov, V.: A
531 35-GHz polarimetric doppler radar for long-term observations of cloud parameters—description of
532 system and data processing, *J. Atmos. Ocean. Tech.*, 32, 675–690,
533 <https://doi.org/10.1175/JTECH-D-14-00066.1>, 2015.

534 Granados-Muñoz, M. J., Navas-Guzmán, F., Bravo-Aranda, J. A., Guerrero-Rascado, J. L., Lyamani, H.,
535 Fernández-Gálvez, J., and Alados-Arboledas, L.: Automatic determination of the planetary boundary
536 layer height using lidar: One-year analysis over southeastern Spain, *J. Geophys. Res.-Atmos.*, 117,
537 <https://doi.org/10.1029/2012JD017524>, 2012.

538 Grossman and Robert, L.: Observed effects of horizontal radiative surface temperature variations on the
539 atmosphere over a midwest watershed during CASES 97, *J. Geophys. Res.-Atmos.*, 110,
540 <https://doi.org/10.1029/2004JD004542>, 2005.

541 Guo, J., Miao, Y., Zhang, Y., Liu, H., Li, Z., Zhang, W., He, J., Lou, M., Yan, Y., Bian, L., and Zhai, P.: The
542 climatology of planetary boundary layer height in China derived from radiosonde and reanalysis data,
543 *Atmos. Chem. Phys.*, 16, 13309–13319, <https://doi.org/10.5194/acp-16-13309-2016>, 2016.

544 Guo, J., Su, T., Li, Z., Miao, Y., Li, J., Liu, H., Xu, H., Cribb, M., and Zhai, P.: Declining frequency of
545 summertime local-scale precipitation over eastern China from 1970 to 2010 and its potential link to
546 aerosols, *Geophys. Res. Lett.*, 44, 5700–5708, <https://doi.org/10.1002/2017GL073533>, 2017.

547 Guo, J., Zhang, J., Yang, K., Liao, H., Zhang, S., Huang, K., Lv, Y., Shao, J., Yu, T., Tong, B., Li, J., Su, T.,
548 Yim, S. H. L., Stoffelen, A., Zhai, P., and Xu, X.: Investigation of near-global daytime boundary layer
549 height using high-resolution radiosondes: first results and comparison with ERA5, MERRA-2, JRA-55,

550 and NCEP-2 reanalyses, *Atmos. Chem. Phys.*, 21, 17079–17097,
551 <https://doi.org/10.5194/acp-21-17079-2021>, 2021.

552 Guo, X., Huang, K., Fang, J., Zhang, Z., Cao, R., Yi, F.: Seasonal and diurnal changes of air temperature and
553 water vapor observed with a microwave radiometer in Wuhan, China, *Remote Sens.-Basel*, 15, 5422.
554 <https://doi.org/10.3390/rs15225422>, 2023.

555 Heus, T., Van Heerwaarden, C. C., Jonker, H. J. J., Pier Siebesma, A., Axelsen, S., Van Den Dries, K.,
556 Geoffroy, O., Moene, A. F., Pino, D., De Roode, S. R., and Vilà-Guerau De Arellano, J.: Formulation of
557 the Dutch Atmospheric Large-Eddy Simulation (DALES) and overview of its applications, *Geosci.*
558 *Model Dev.*, 3, 415–444, <https://doi.org/10.5194/gmd-3-415-2010>, 2010.

559 Holtslag, A. A. M. and Nieuwstadt, F. T. M.: Scaling the atmospheric boundary layer, *Bound.-Lay. Meteorol.*,
560 36, 201–209, <https://doi.org/10.1007/BF00117468>, 1986.

561 Huang, M., Gao, Z., Miao, S., Chen, F., LeMone, M. A., Li, J., Hu, F., and Wang, L.: Estimate of
562 boundary-layer depth over Beijing, China, using doppler lidar data during SURF-2015, *Bound.-Lay.*
563 *Meteorol.*, 162, 503–522, <https://doi.org/10.1007/s10546-016-0205-2>, 2017.

564 Immler, F. and Schrems, O.: Vertical profiles, optical and microphysical properties of Saharan dust layers
565 determined by a ship-borne lidar, *Atmos. Chem. Phys.*, <https://doi.org/10.5194/acp-3-1353-2003>, 2003.

566 Klett, J. D.: Stable analytical inversion solution for processing lidar returns, *Appl. Opt.*, 20, 211–220,
567 <https://doi.org/10.1364/AO.20.000211>, 1981.

568 Kong, W. and Yi, F.: Convective boundary layer evolution from lidar backscatter and its relationship with
569 surface aerosol concentration at a location of a central China megacity, *J. Geophys. Res.-Atmos.*, 120,
570 7928–7940, <https://doi.org/10.1002/2015JD023248>, 2015.

571 Kotthaus, S., Bravo-Aranda, J. A., Collaud Coen, M., Guerrero-Rascado, J. L., Costa, M. J., Cimini, D.,
572 O'Connor, E. J., Hervo, M., Alados-Arboledas, L., Jiménez-Portaz, M., Mona, L., Ruffieux, D.,

573 Illingworth, A., and Haeffelin, M.: Atmospheric boundary layer height from ground-based remote
574 sensing: a review of capabilities and limitations, *Atmos. Meas. Tech.*, 16, 433–479,
575 <https://doi.org/10.5194/amt-16-433-2023>, 2023.

576 Kwon, H.-G., Yang, H., and Yi, C.: Study on radiative flux of road resolution during winter based on local
577 weather and topography, *Remote Sens.-Basel*, 14, 6379, <https://doi.org/10.3390/rs14246379>, 2022.

578 Lammert, A. and Bösenberg, J.: Determination of the convective boundary-layer height with laser remote
579 sensing, *Bound.-Lay. Meteorol.*, 119, 159–170, <https://doi.org/10.1007/s10546-005-9020-x>, 2006.

580 LeMone, M. A., Chen, F., Tewari, M., Dudhia, J., Geerts, B., Miao, Q., Coulter, R. L., and Grossman, R. L.:
581 Simulating the IHOP_2002 fair-weather CBL with the WRF-ARW–Noah modeling system. Part I:
582 Surface fluxes and CBL structure and evolution along the eastern track, *Mon. Weather Rev.*, 138,
583 722–744, <https://doi.org/10.1175/2009MWR3003.1>, 2010.

584 Lewis, J., E. J. Welton, A. M. Molod, and E. Joseph: Improved boundary layer depth retrievals from
585 MPLNET, *J. Geophys. Res.-Atmos.*, 118, 9870–9879, <https://doi.org/10.1002/jgrd.50570>, 2013.

586 Li, H., Yang, Y., Hu, X., Huang, Z., Wang, G., Zhang, B., and Zhang, T.: Evaluation of retrieval methods of
587 daytime convective boundary layer height based on lidar data, *J. Geophys. Res.-Atmos.*, 122,
588 4578–4593, <https://doi.org/10.1002/2016JD025620>, 2017.

589 Liu, B., Ma, Y., Guo, J., Gong, W., Zhang, Y., Mao, F., Li, J., Guo, X., and Shi, Y.: Boundary layer heights as
590 derived from ground-based radar wind profiler in Beijing, *IEEE T. Geosci. Remote*, 57, 8095–8104,
591 <https://doi.org/10.1109/TGRS.2019.2918301>, 2019.

592 Liu, F., Yi, F., Yin, Z., Zhang, Y., He, Y., and Yi, Y.: Measurement report: characteristics of clear-day
593 convective boundary layer and associated entrainment zone as observed by a ground-based polarization
594 lidar over Wuhan (30.5° N, 114.4° E), *Atmos. Chem. Phys.*, 21, 2981–2998,
595 <https://doi.org/10.5194/acp-21-2981-2021>, 2021.

596 Liu, S. and Liang, X.-Z.: Observed diurnal cycle climatology of planetary boundary layer height, *J. Climate*,
597 23, 5790–5809, <https://doi.org/10.1175/2010JCLI3552.1>, 2010.

598 Mahrt, L.: Stratified atmospheric boundary layers, *Bound.-Lay. Meteorol.*, 90, 375–396,
599 <https://doi.org/10.1023/A:1001765727956>, 1999.

600 Manninen, A. J., Marke, T., Tuononen, M., and O’Connor, E. J.: Atmospheric boundary layer classification
601 with doppler lidar, *J. Geophys. Res.-Atmos.*, 123, 8172–8189, <https://doi.org/10.1029/2017JD028169>,
602 2018.

603 Mao, Z., Huang, K., Fang, J., Zhang, Z., Cao, R., and Yi, F.: An Observation of precipitation during cooling
604 with Ka-Band cloud radar in Wuhan, China, *Remote Sens.-Basel*, 15, 5397,
605 <https://doi.org/10.3390/rs15225397>, 2023.

606 Martucci, G., R. Matthey, V. Mitev, and H. Richner: Comparison between backscatter lidar and radiosonde
607 measurements of the diurnal and nocturnal stratification in the lower troposphere, *J. Atmos. Ocean.*
608 *Tech.*, 24, 1231–1244, <https://doi.org/10.1175/JTECH2036.1>, 2007.

609 Moran, K. P., Martner, B. E., Post, M. J., Kropfli, R. A., Welsh, D. C., and Widener, K. B.: An unattended
610 cloud-profiling radar for use in climate research, *B. Am. Meteorol. Soc.*, 79, 443–455,
611 [https://doi.org/10.1175/1520-0477\(1998\)079<0443:AUCPRF>2.0.CO;2](https://doi.org/10.1175/1520-0477(1998)079<0443:AUCPRF>2.0.CO;2), 1998.

612 Neggers, R. A. J., Siebesma, A. P., Lenderink, G., and Holtslag, A. A. M.: An evaluation of mass flux
613 closures for diurnal cycles of shallow cumulus, *Mon. Weather Rev.*, 132, 2525–2538,
614 <https://doi.org/10.1175/MWR2776.1>, 2004.

615 Pal, S., Behrendt, A., and Wulfmeyer, V.: Elastic-backscatter-lidar-based characterization of the convective
616 boundary layer and investigation of related statistics, *Ann. Geophys.-Italy*, 28, 825–847,
617 <https://doi.org/10.5194/angeo-28-825-2010>, 2010.

618 Pal, S., Lopez, M., Schmidt, M., Ramonet, M., Gibert, F., Xueref-Remy, I., and Ciais, P.: Investigation of the

619 atmospheric boundary layer depth variability and its impact on the ^{222}Rn concentration at a rural site
620 in France, *J. Geophys. Res.-Atmos.*, 120, 623–643, <https://doi.org/10.1002/2014JD022322>, 2015.

621 Pearson, G., Davies, F., and Collier, C.: Remote sensing of the tropical rain forest boundary layer using
622 pulsed Doppler lidar, *Atmos. Chem. Phys.*, 10, 5891–5901, <https://doi.org/10.5194/acp-10-5891-2010>,
623 2010.

624 Piironen, A. K. and Eloranta, E. W.: Convective boundary layer mean depths and cloud geometrical
625 properties obtained from volume imaging lidar data, *J. Geophys. Res.-Atmos.*, 100, 25569–25576,
626 <https://doi.org/10.1029/94JD02604>, 1995.

627 Ribeiro, F. N. D., Oliveira, A. P. D., Soares, J., Miranda, R. M. D., Barlage, M., and Chen, F.: Effect of sea
628 breeze propagation on the urban boundary layer of the metropolitan region of Sao Paulo, Brazil, *Atmos.*
629 *Res.*, 214, 174–188, <https://doi.org/10.1016/j.atmosres.2018.07.015>, 2018.

630 Sandeep, A., Rao, T. N., Ramkiran, C. N., and Rao, S. V. B.: Differences in atmospheric boundary-layer
631 characteristics between wet and dry episodes of the Indian summer monsoon, *Bound.-Lay. Meteorol.*,
632 153, 217–236, <https://doi.org/10.1007/s10546-014-9945-z>, 2014.

633 Schneider, S. P.: Effects of roughness on hypersonic boundary-layer transition, *J. Spacecraft Rockets*, 45,
634 193–209, <https://doi.org/10.2514/1.29713>, 2008.

635 Schween, J. H., Hirsikko, A., Löhnert, U., and Crewell, S.: Mixing-layer height retrieval with ceilometer and
636 Doppler lidar: from case studies to long-term assessment, *Atmos. Meas. Tech.*, 7, 3685–3704,
637 <https://doi.org/10.5194/amt-7-3685-2014>, 2014.

638 Seibert, P.: Review and intercomparison of operational methods for the determination of the mixing height,
639 *Atmos. Environ.*, 34, 1001–1027, [https://doi.org/10.1016/S1352-2310\(99\)00349-0](https://doi.org/10.1016/S1352-2310(99)00349-0), 2000.

640 Seidel, D. J., Ao, C. O., and Li, K.: Estimating climatological planetary boundary layer heights from
641 radiosonde observations: Comparison of methods and uncertainty analysis, *J. Geophys. Res.-Atmos.*,

642 115, 2009JD013680, <https://doi.org/10.1029/2009JD013680>, 2010.

643 Seidel, D. J., Zhang, Y., Beljaars, A., Golaz, J., Jacobson, A. R., and Medeiros, B.: Climatology of the
644 planetary boundary layer over the continental United States and Europe, *J. Geophys. Res.-Atmos.*, 117,
645 2012JD018143, <https://doi.org/10.1029/2012JD018143>, 2012.

646 Singh, N., Solanki, R., Ojha, N., Janssen, R. H. H., Pozzer, A., and Dhaka, S. K.: Boundary layer evolution
647 over the central Himalayas from radio wind profiler and model simulations, *Atmos. Chem. Phys.*, 16,
648 10559–10572, <https://doi.org/10.5194/acp-16-10559-2016>, 2016.

649 Solanki, R., Guo, J., Li, J., Singh, N., Guo, X., Han, Y., Lv, Y., Zhang, J., and Liu, B.:
650 Atmospheric-boundary-layer-height variation over mountainous and urban sites in Beijing as derived
651 from radar wind-profiler measurements, *Bound.-Lay. Meteorol.*, 181, 125–144,
652 <https://doi.org/10.1007/s10546-021-00639-9>, 2021.

653 Stull, R. B.: *An Introduction to Boundary Layer Meteorology*, Springer Netherlands, Dordrecht,
654 <https://doi.org/10.1007/978-94-009-3027-8>, 1988.

655 Su, T., Li, Z., and Kahn, R.: A new method to retrieve the diurnal variability of planetary boundary layer
656 height from lidar under different thermodynamic stability conditions, *Remote Sens.-Basel Environ.*,
657 237, 111519, <https://doi.org/10.1016/j.rse.2019.111519>, 2020.

658 Tang, G., Zhang, J., Zhu, X., Song, T., Munkel, C., Hu, B., Schäfer, K., Liu, Z., Zhang, J., Wang, L., Xin, J.,
659 Suppan, P., and Wang, Y.: Mixing layer height and its implications for air pollution over Beijing, China,
660 *Atmos. Chem. Phys.*, 16, 2459–2475, <https://doi.org/10.5194/acp-16-2459-2016>, 2016.

661 Tennekes, H. and Driedonks, A. G. M.: Basic entrainment equations for the atmospheric boundary layer,
662 *Bound.-Lay. Meteorol.*, 20, 515–531, <https://doi.org/10.1007/BF00122299>, 1981.

663 Träumner, K., Kottmeier, C., Corsmeier, U., and Wieser, A.: Convective boundary-layer entrainment: short
664 review and progress using doppler lidar, *Bound.-Lay. Meteorol.*, 141, 369–391,

665 <https://doi.org/10.1007/s10546-011-9657-6>, 2011.

666 Tucker, S. C., Senff, C. J., Weickmann, A. M., Brewer, W. A., Banta, R. M., Sandberg, S. P., Law, D. C., and
667 Hardesty, R. M.: Doppler lidar estimation of mixing height using turbulence, shear, and aerosol profiles,
668 *J. Atmos. Ocean. Tech.*, 26, 673–688, <https://doi.org/10.1175/2008JTECHA1157.1>, 2009.

669 Van Der Kamp, D. and McKendry, I.: Diurnal and seasonal trends in convective mixed-layer heights
670 estimated from two years of continuous ceilometer observations in Vancouver, BC, *Bound.-Lay.*
671 *Meteorol.*, 137, 459–475, <https://doi.org/10.1007/s10546-010-9535-7>, 2010.

672 Yang, T., Wang, Z., Zhang, W., Gbaguidi, A., Sugimoto, N., Wang, X., Matsui, I., and Sun, Y.: Technical
673 note: Boundary layer height determination from lidar for improving air pollution episode modeling:
674 development of new algorithm and evaluation, *Atmos. Chem. Phys.*, 17, 6215–6225,
675 <https://doi.org/10.5194/acp-17-6215-2017>, 2017.

676 Yates, D. N., Chen, F., Lemone, M. A., Qualls, R., Oncley, S. P., and Gross, R. L.: A cooperative
677 atmosphere-surface exchange study (CASES) dataset for analyzing and parameterizing the effects of
678 land surface heterogeneity on area-averaged surface heat fluxes, *J. Appl. Meteorol.*, 40,
679 [https://doi.org/10.1175/1520-0450\(2001\)040<0921:ACASES>2.0.CO;2](https://doi.org/10.1175/1520-0450(2001)040<0921:ACASES>2.0.CO;2), 2001.

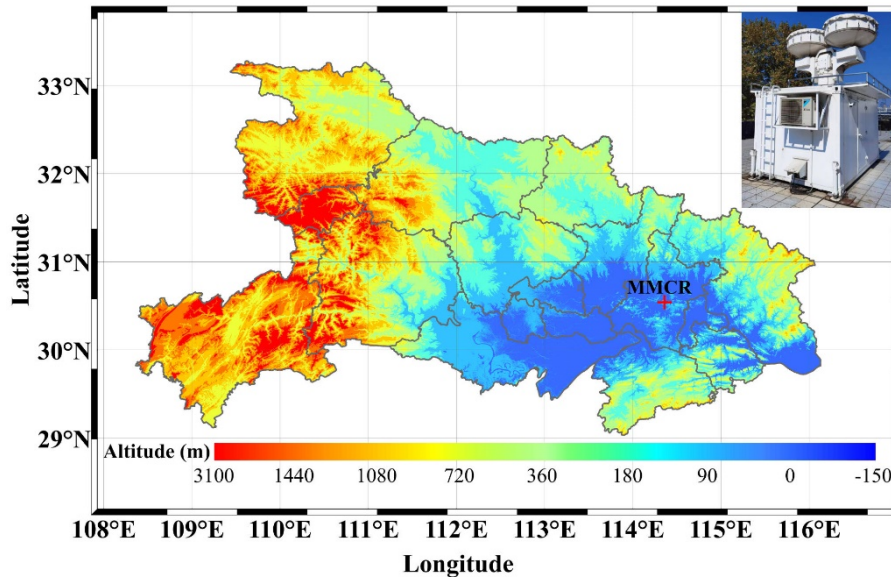
680 Zhang, H., Zhou, X., Zou, J., Wang, W., Xue, L., Ding, Q., Wang, X., Zhang, N., Ding, A., Sun, J., and
681 Wang, W.: A review on the methods for observing the substance and energy exchange between
682 atmosphere boundary layer and free troposphere, *Remote Sens.-Basel*, 15, 5397,
683 <https://doi.org/10.3390/rs15225397>, 2018.

684 Zhang, J., Guo, J., Li, J., Zhang, S., Tong, B., Shao, J., Li, H., Zhang, Y., Cao, L., Zhai, P., Xu, X., and Wang,
685 M.: A Climatology of merged daytime planetary boundary layer height over China from radiosonde
686 measurements, *J. Geophys. Res.-Atmos.*, 127, e2021JD036367, <https://doi.org/10.1029/2021JD036367>,

687 2022.

688 Zhang, M., Tian, P., Zeng, H., Wang, L., Liang, J., Cao, X., and Zhang, L.: A comparison of wintertime
689 atmospheric boundary layer heights determined by tethered balloon soundings and lidar at the site of
690 SACOL, *Remote Sens.-Basel*, 13, 1781, <https://doi.org/10.3390/rs13091781>, 2021.

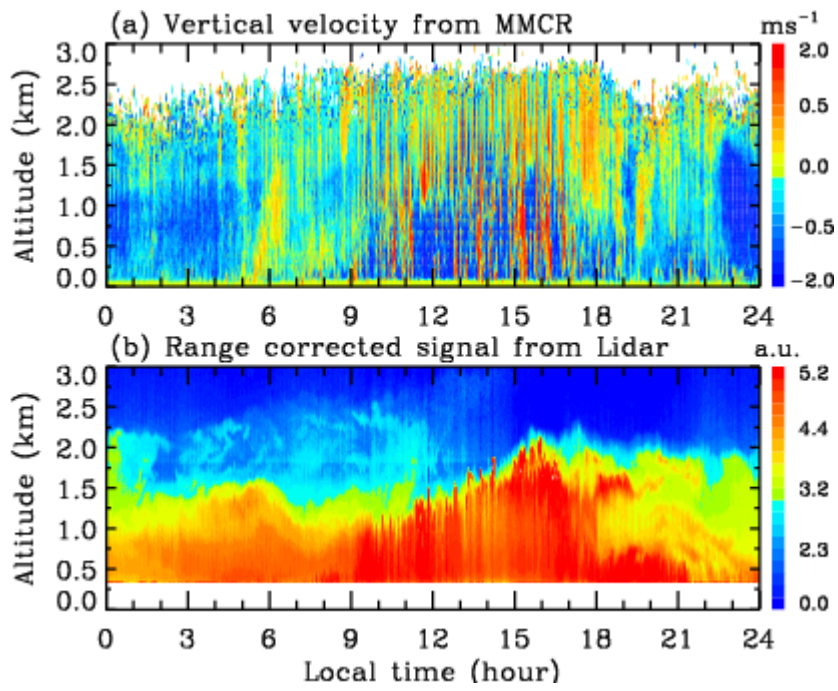
691 Zhang, Y., Zhang, S., Huang, C., Huang, K., Gong, Y., and Gan, Q.: Diurnal variations of the planetary
692 boundary layer height estimated from intensive radiosonde observations over Yichang, China, *Sci.*
693 *China Technol. Sc.*, 57, 2172–2176, <https://doi.org/10.1007/s11431-014-5639-5>, 2014.



694

695 **Figure 1.** Topographic elevation map of Hubei Province and Ka-band MMCR located in Wuhan University

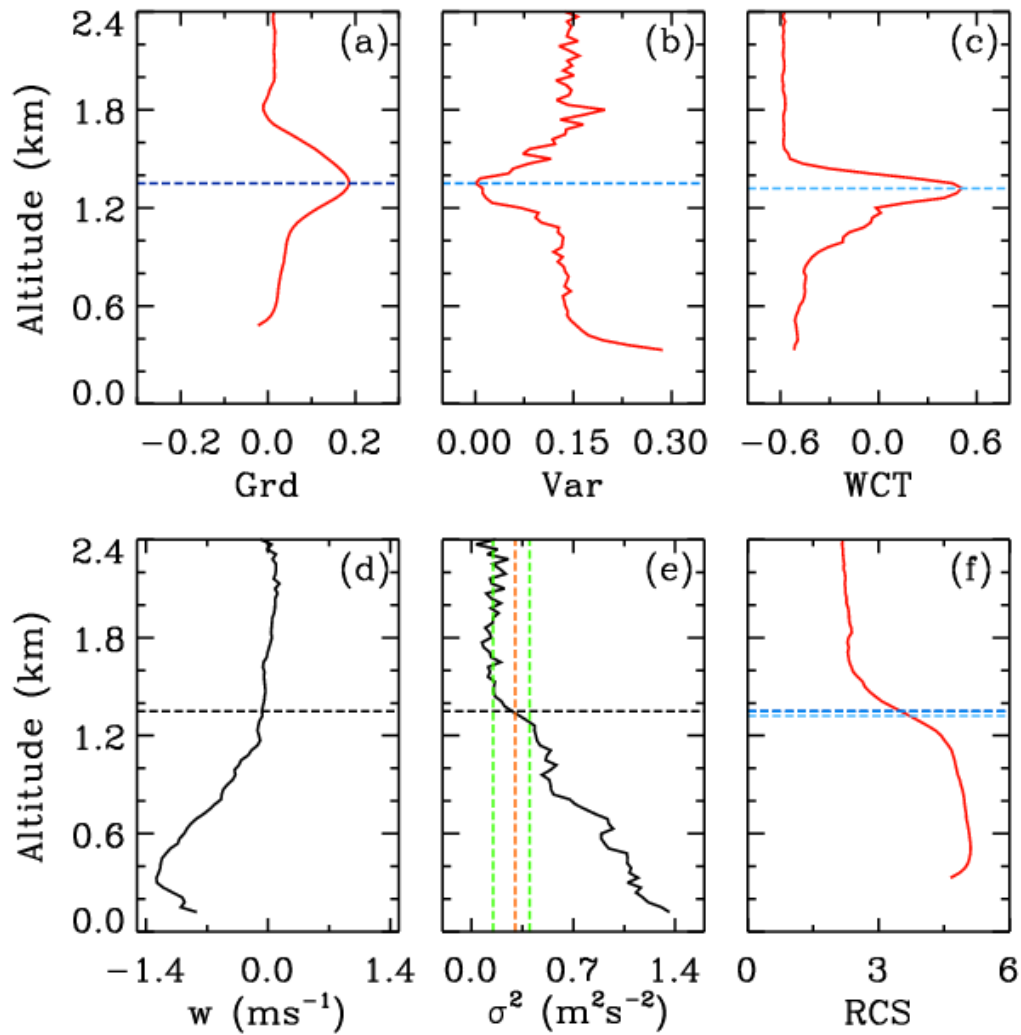
696 (30.54°N, 114.36°E). The red crisscross denotes the site of MMCR.



697

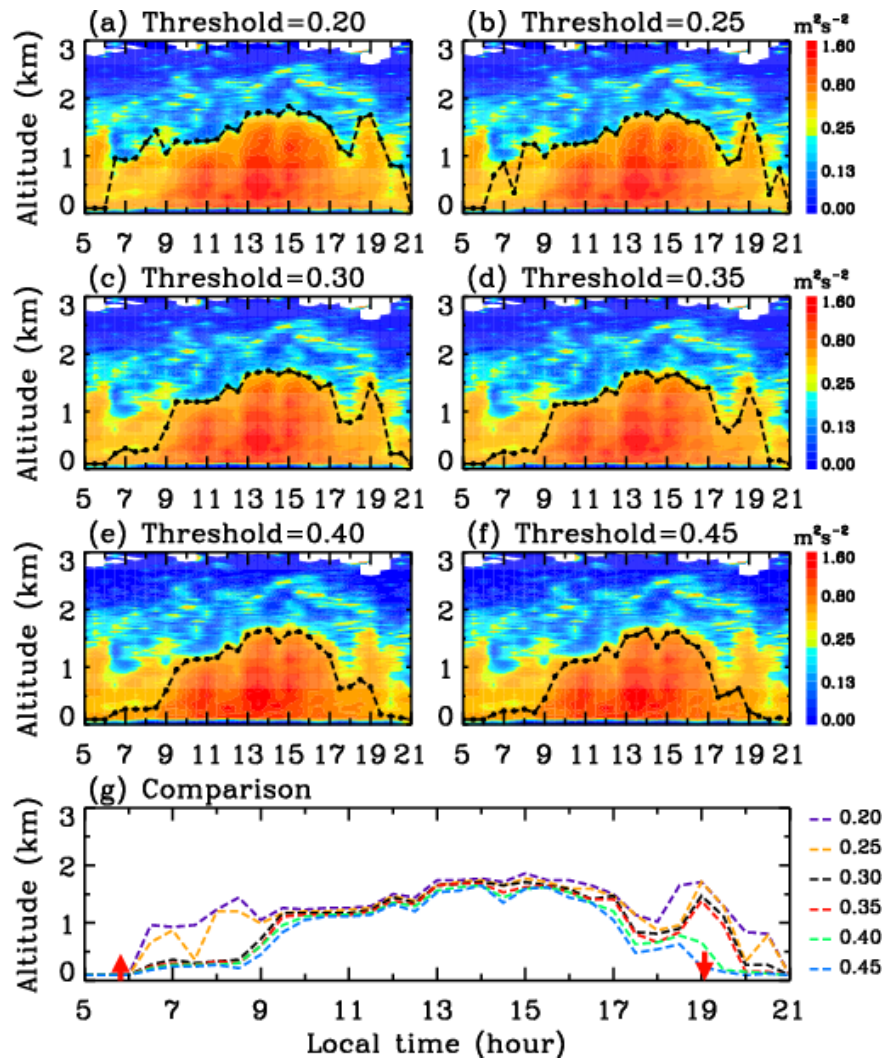
698 **Figure 2.** Time-height section of (a) vertical velocity from MMCR and (b) RCS from lidar on 15 August

699 2020.



700

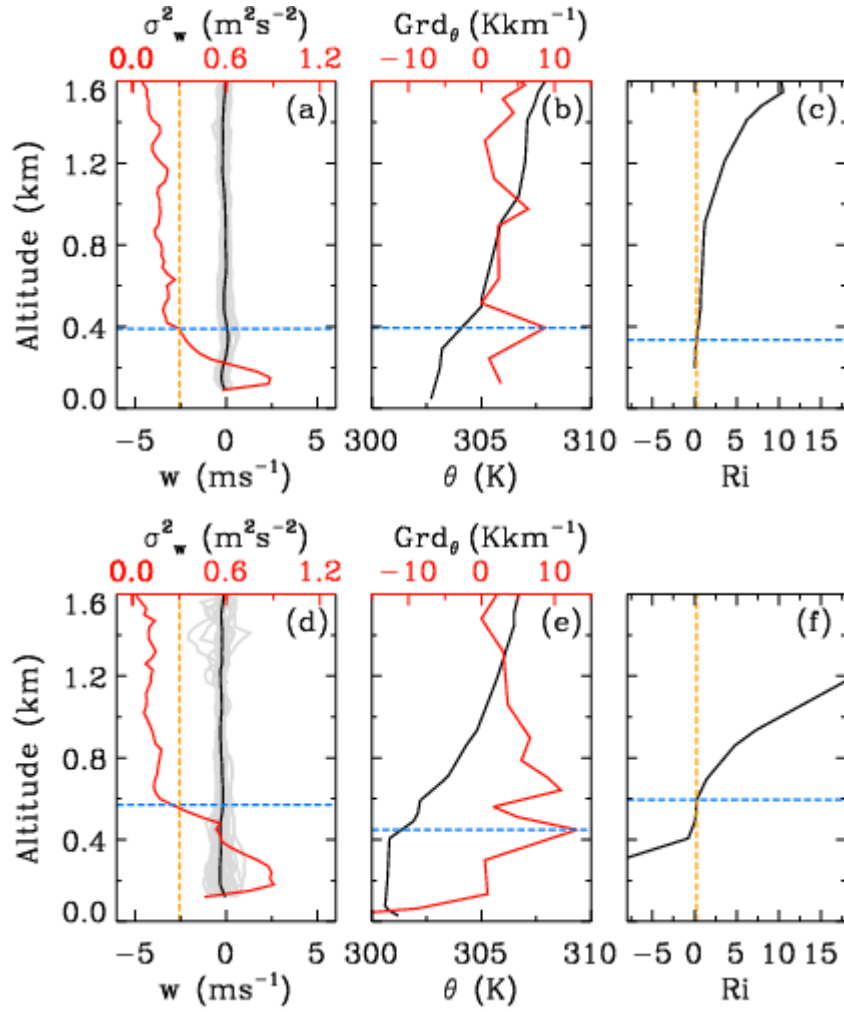
701 **Figure 3.** Profiles of (a) RCS gradient, (b) variance, (c) WCT and (f) RCS from lidar, and (d) vertical
 702 vertical velocity and (e) its variance from MMCR between 12:15 and 12:45 LT on 15 August 2020. In these panels,
 703 the horizontal lines in different colors represent the CBLH determined by different methods. In Panel 3e, the
 704 orange vertical line denotes the selected threshold of $0.3 \text{ m}^2 \text{ s}^{-2}$, and the two green vertical lines correspond
 705 to the variances of 0.15 and $0.4 \text{ m}^2 \text{ s}^{-2}$, respectively.



706

707 **Figure 4.** CBLHs derived from thresholds of (a) 0.2, (b) 0.25, (c) 0.3, (d) 0.35, (e) 0.4 and (f) 0.45 $\text{m}^2 \text{s}^{-2}$
 708 superimposed over vertical velocity variance (color shading) from MMCR on 15 August 2020, and (g) their
 709 comparison. In Panel 4g, the two red arrows denote the time of sunrise and sunset at 05:50 and 19:05,
 710 respectively.

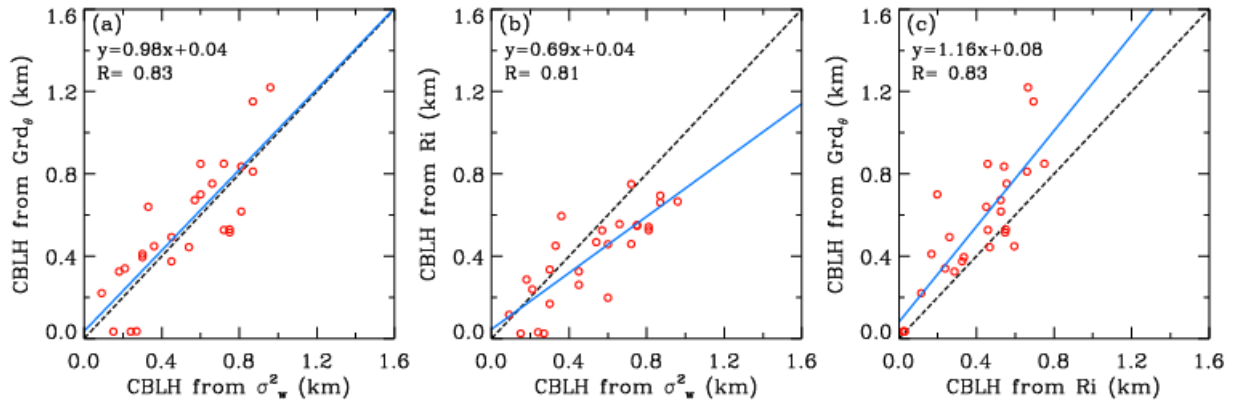
711



712

713 **Figure 5.** Comparison of CBLHs estimated by (a, d) threshold of $\sigma_w^2=0.3 \text{ m}^2 \text{ s}^{-2}$ from MMCR, and (b, e)
 714 maximum gradient of θ and (c, f) threshold of $Ri=0.25$ from radiosonde data at 08:00 on (upper) 21 and
 715 (lower) 25 July 2021. In the panels 5a and 5d, the gray and black lines denote (lower horizontal axis) w and its
 716 mean value from MMCR, respectively, and the red and yellow lines denote (upper horizontal axis) σ_w^2 and the
 717 threshold of $\sigma_w^2=0.3 \text{ m}^2 \text{ s}^{-2}$, respectively. In the panels 5b and 5e, the black and red lines denote (lower
 718 horizontal axis) θ and (upper horizontal axis) its gradient from radiosonde, respectively. In the panels 5c and
 719 5f, the black and yellow lines denote Ri and the threshold of $Ri=0.25$ from radiosonde data, respectively.
 720 The blue horizontal line represents the position of identified CBL top.

721



722

723

Figure 6. Scatterplot of CBLHs derived from (a) threshold of $\sigma_w^2=0.3 \text{ m}^2 \text{ s}^{-2}$ from MMCR vs. maximum

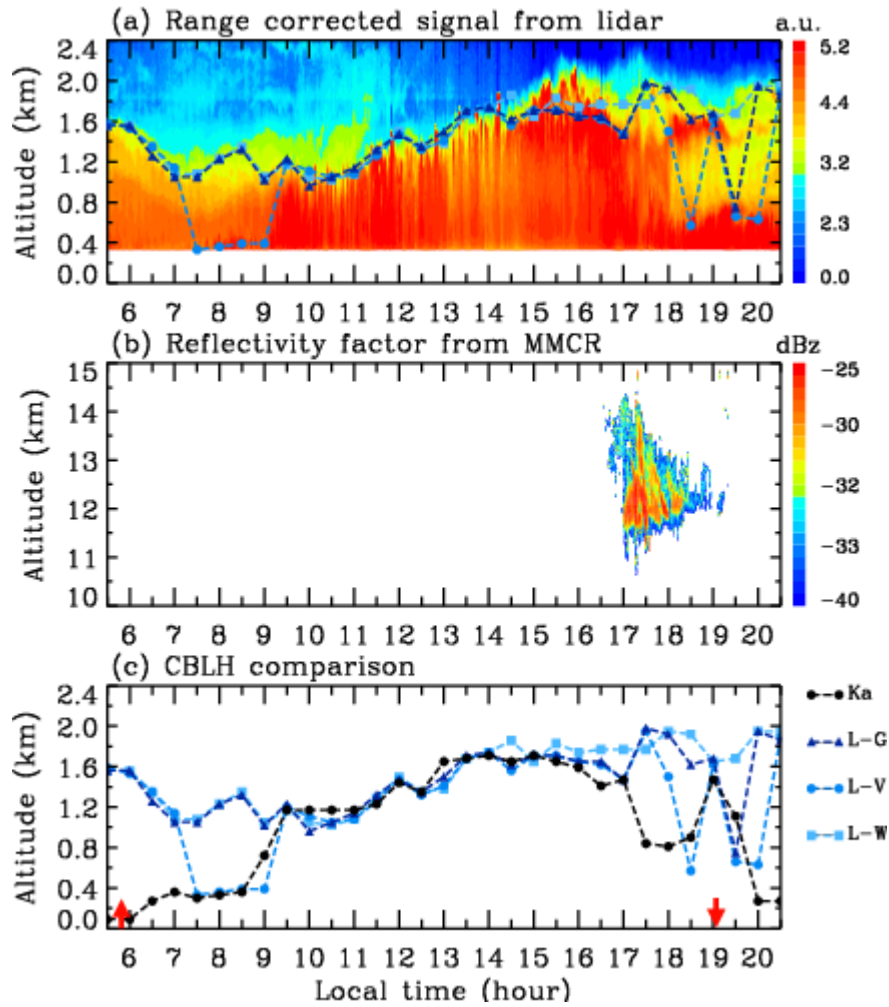
724

gradient of θ from radiosonde, (b) threshold of $\sigma_w^2=0.3 \text{ m}^2 \text{ s}^{-2}$ from MMCR vs. threshold of $Ri=0.25$ from

725

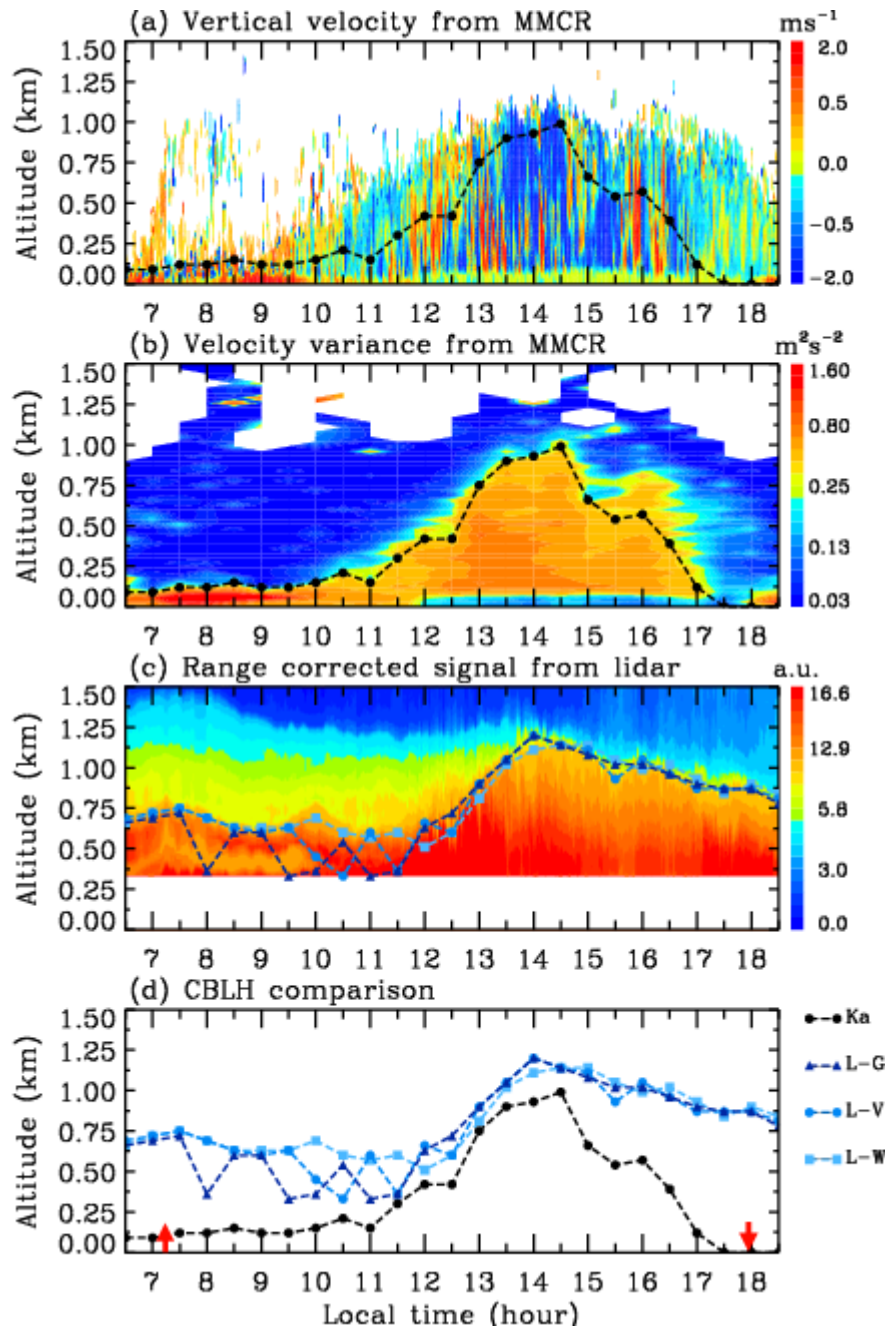
radiosonde, and (c) threshold of $Ri=0.25$ vs. maximum gradient of θ from radiosonde.

726



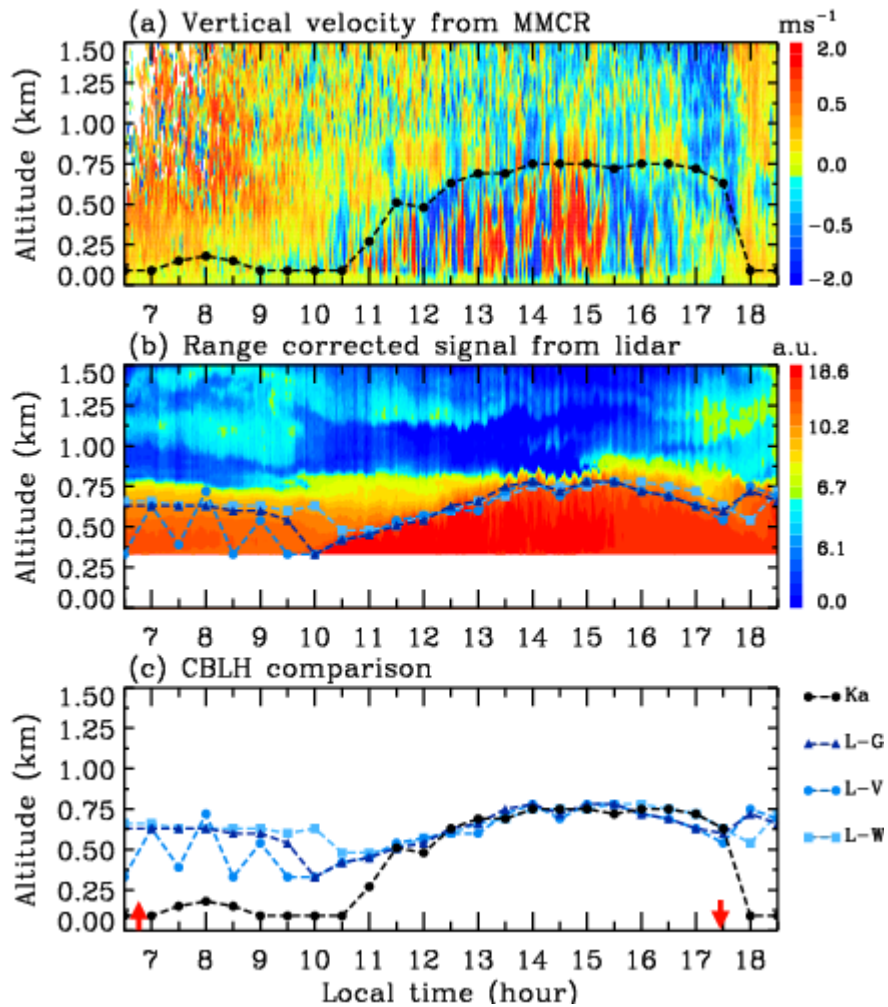
727

728 **Figure 7.** (a) Evolution of CBLH derived from RCS gradient, variance and WCT superimposed over lidar
 729 RCS (color shading) on 15 August 2020, (b) reflectivity factor from MMCR, and (c) comparison of CBLHs
 730 derived from MMCR and lidar observations. The black dash curve with circle (Ka) denotes the CBLH
 731 determined by the variance threshold of $0.3 \text{ m}^2 \text{ s}^{-2}$ in the Ka-band MMCR observation, while the dark blue,
 732 blue and light blue dash curves with triangle (L-G), circle (L-V) and square (L-W) represent the CBLH
 733 determined by the gradient, variance and WCT in the lidar measurement, respectively. In Panel 5c, the two
 734 red arrows denote the time of sunrise and sunset at 05:50 and 19:05, respectively.



735

736 **Figure 8.** Distributions of (a) vertical velocity and (b) its variance from MMCR and (c) lidar RCS on 31
 737 January 2020 with retrieved CBLH, and (d) comparison of CBLHs derived from MMCR and lidar
 738 observations. The threshold of vertical velocity variance from the MMCR is $0.3 \text{ m}^2 \text{ s}^{-2}$. In Panel 6d, the two
 739 red arrows denote the time of sunrise and sunset at 07:15 and 17:57, respectively.



740

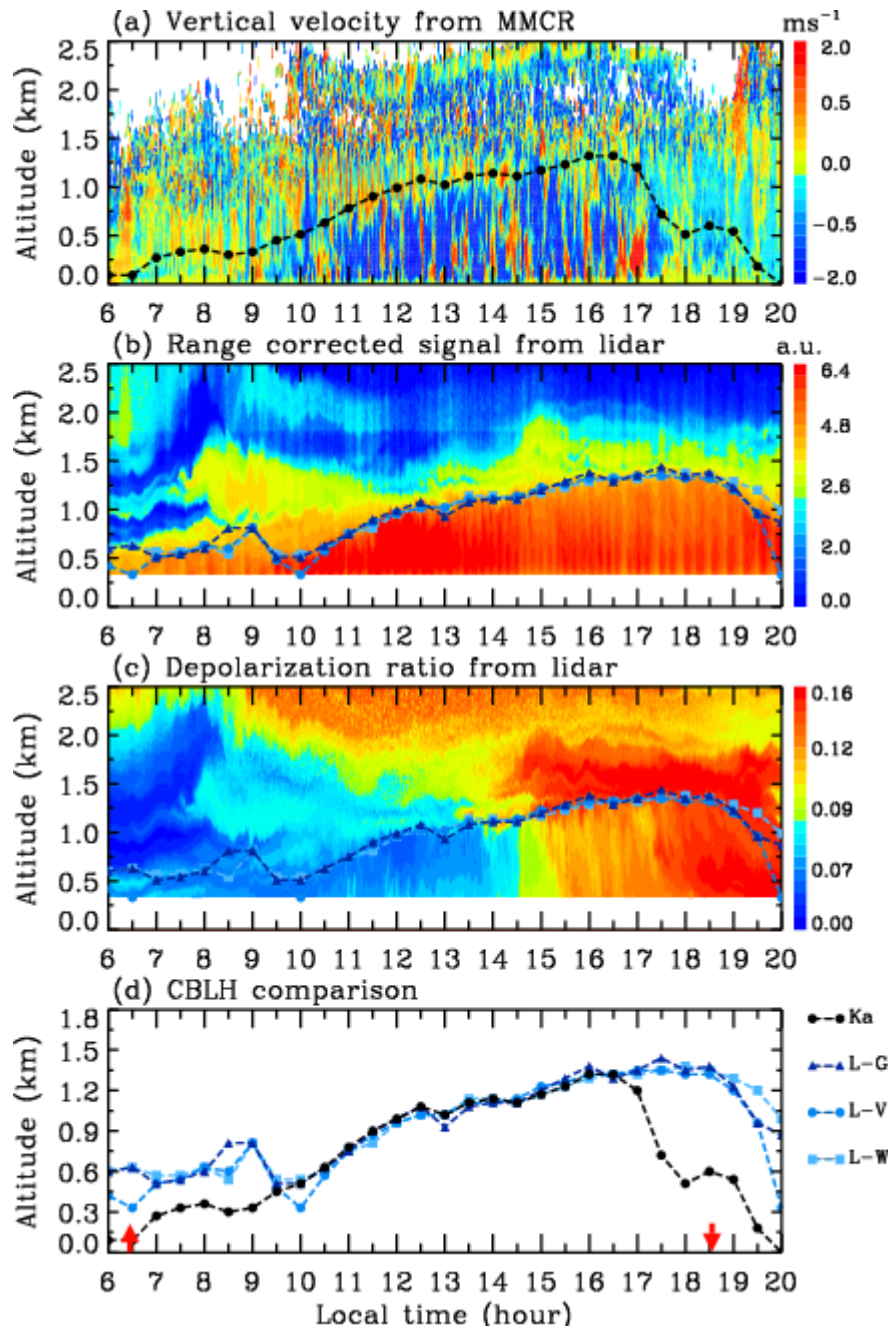
741

742

743

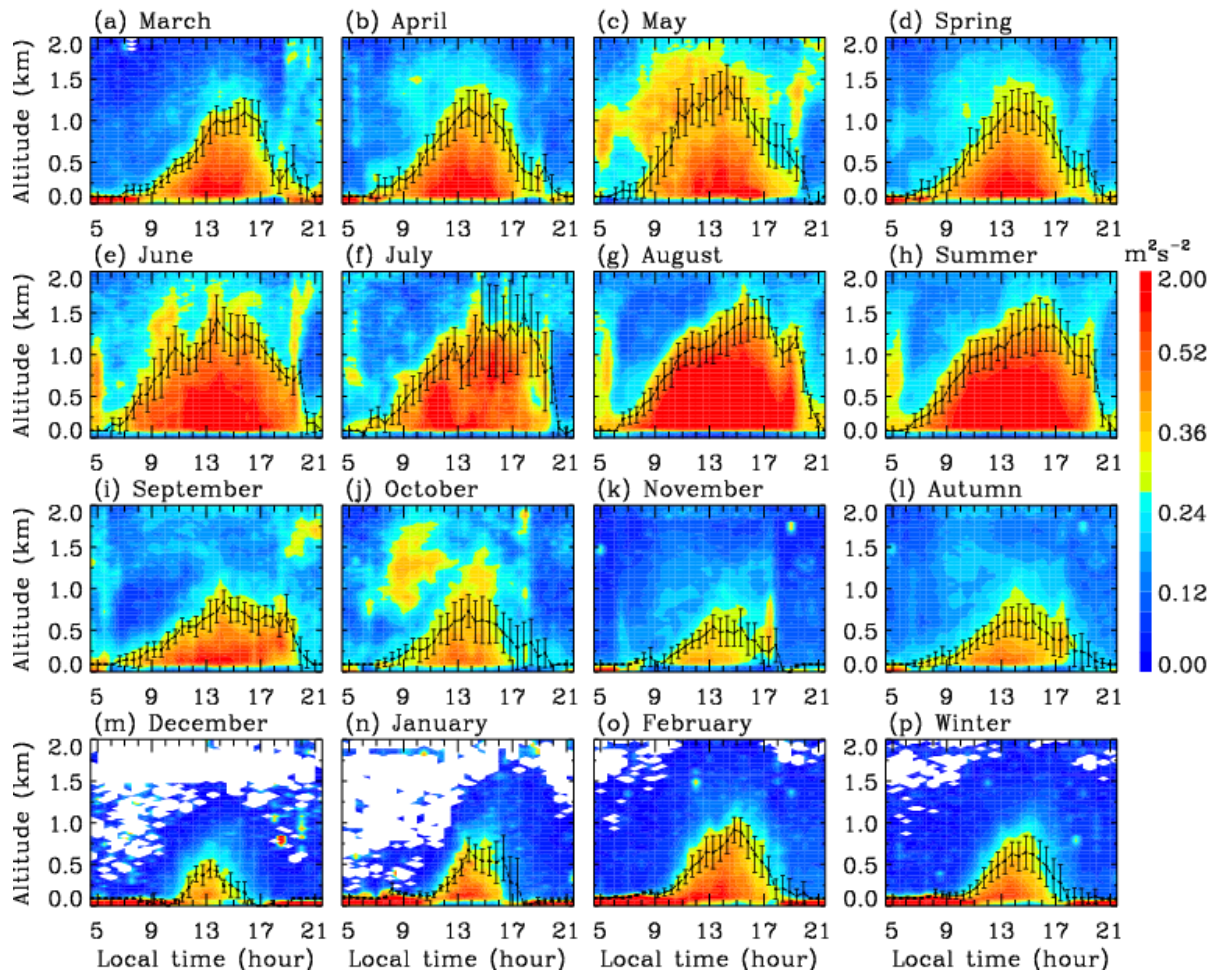
744

Figure 9. Distributions of (a) vertical velocity from MMCR and (b) lidar RCS on 12 November 2020 with retrieved CBLH, and (c) comparison of CBLHs derived from MMCR and lidar observations. The threshold of vertical velocity variance from the MMCR is $0.3 \text{ m}^2 \text{ s}^{-2}$. In Panel 7c, the two red arrows denote the time of sunrise and sunset at 06:47 and 17:27, respectively.



745

746 **Figure 10.** Distributions of (a) vertical velocity from MMCR and lidar (b) RCS and (c) depolarization ratio
 747 on 19 March 2020 with retrieved CBLH, and (d) comparison of CBLHs derived from MMCR and lidar
 748 observations. The threshold of vertical velocity variance from the MMCR is $0.3 \text{ m}^2 \text{ s}^{-2}$. In Panel 8d, the two
 749 red arrows denote the time of sunrise and sunset at 06:27 and 18:34, respectively.



750

751 **Figure 11.** Monthly and seasonal mean values and statistical standard deviations of CBLH estimated by
 752 threshold of vertical velocity variance from MMCR. The variance threshold is $0.3 \text{ m}^2 \text{ s}^{-2}$, and the color shading
 753 denotes the variance distribution. The months and seasons are marked above the corresponding panels,
 754 respectively.